Check for updates

A graphene–Mo$_2$C heterostructure for a highly responsive broadband photodetector†

Xiaozhi Bao,[a] Tian Sun,[b] Yan Liu,[b] Chuan Xu,[c] Weiliang Ma,[b] Junpo Guo,[a] Yun Zheng,[a] Shivananju Bannur Nanjunda,[d] Huating Liu,[e] Zongyu Huang,[e] Shaojuan Li,[bf] Shenghuang Lin,[g] Guichuan Xing,[a] Wencai Ren,*[c] Qiaoliang Bao*[b] and Huaiyu Shao*[a]

Photodetectors based on intrinsic graphene can operate over a broad wavelength range with ultrafast response, but their responsivity is much lower than commercial silicon photodiodes. The combination of graphene with two-dimensional (2D) semiconductors may enhance the light absorption, but there is still a cutoff wavelength originating from the bandgap of semiconductors. Here, we report a highly responsive broadband photodetector based on the heterostructure of graphene and transition metal carbides (TMCs, more specifically Mo$_2$C). The graphene–Mo$_2$C heterostructure enhanced light absorption over a broad wavelength range from ultraviolet to infrared. In addition, there is very small resistance for photoexcited carriers in both graphene and Mo$_2$C. Consequently, photodetectors based on the graphene–Mo$_2$C heterostructure deliver a very high responsivity from visible to infrared telecommunication wavelengths.

Owing to its unique band structure with the zero bandgap and linear dispersion near Dirac point, graphene holds great potential for many broadband photonic and optoelectronic device applications such as broadband polarizers,[1] broadband modulators,[2] transparent electrodes[3] and broadband photodetectors.[4–6] One atomic layer graphene can absorb ∼2.3% of incident light[7] over a broadband wavelength from ultraviolet to terahertz. In addition, graphene also shows high carrier mobility (up to 200 000 cm^2 V^{-1} S^{-1})[8,9] and fast photoelectric response (up to 40 GHz),[6] which makes graphene a promising candidate for ultra-fast and ultra-broadband photodetection. Nevertheless, the photo-responsivity of an intrinsic graphene photodetector is at the scale of 10 mA W^{-1},[5] which is three orders of magnitude lower than the commercially available silicon-based photodiodes in the visible range, because of the relatively low absolute absorptance and huge recombination of photo-generated carriers. Many efforts have been made to improve the responsivity of the graphene-based photodetector, including the integration of graphene with plasmonic structures[10,11] or microcavities,[12] but the fabrication process is complex, and the responsivity is still as low as several tens of mA W^{-1}.

Other two-dimensional (2D) materials, such as transition metal dichalcogenides (TMDs), are gaining increasing attention as promising channel materials for field-effect transistors (FETs). Monolayer TMDs are direct-bandgap semiconductors,[13] which are suitable for applications in optoelectronic devices because of the high absorption coefficient and efficient electron–hole pair generation under photoexcitation.[14] Constructing van der Waals heterostructures consisting of graphene and TMD is an effective approach to combine the merits of both materials. In particular, graphene–MoS$_2$[15] or graphene–WSe$_2$[16] heterostructure photodetectors have shown unprecedented performance in terms of high responsivity and sensitivity because of the efficient generation of photocarriers by TMDs and high carrier mobility of graphene. However, the large bandgap (1–2.5 eV[17,18]) and relatively low mobility (10–250 cm^2 V^{-1} s^{-1}) in TMDs impede broadband photodetection, particularly in telecommunication bands around 1550 nm.

Recently, 2D transition metal carbides (TMCs) have been synthesized, which have shown amazing optical and electronic

[a] *Guangdong-Hong Kong-Macau Joint Laboratory for Photonic-Thermal-Electrical Energy Materials and Devices, Institute of Applied Physics and Materials Engineering, University of Macau, Avenida da Universidade, Taipa, Macao SAR 999078, China. E-mail: hshao@um.edu.mo*

[b] *Institute of Functional Nano and Soft Materials (FUNSOM), Soochow University, Suzhou 215123, P. R. China. E-mail: qiaoliang.bao@gmail.com*

[c] *Shenyang National Laboratory for Materials Science, Institute of Metal Research, Chinese Academy of Sciences, Shenyang 110016, P. R. China. E-mail: wcren@imr.ac.cn*

[d] *Department of Electrical Engineering, Centre of Excellence in Biochemical Sensing and Imaging Technologies (Cen-Bio-SIM), Indian Institute of Technology Madras, Chennai 600036, India*

[e] *Hunan Key Laboratory for Micro-Nano Energy Materials and Devices, School of Physics and Optoelectronic, Xiangtan University, Hunan 411105, China*

[f] *State Key Laboratory of Applied Optics, Changchun Institute of Optics, Fine Mechanics and Physics, Chinese Academy of Sciences, Changchun, Jilin, 130033, China*

[g] *Songshan Lake Materials Laboratory, Dongguan 523808, China*

† Electronic supplementary information (ESI) available. See DOI: 10.1039/d1cp03536c

23024 | *Phys. Chem. Chem. Phys.*, 2021, **23**, 23024–23031

This journal is © the Owner Societies 2021

properties.[19,20] As a result, from the incorporation of carbon atoms into the metal lattice, transition metal carbides are a large family of materials, which combine the properties of ceramics and metals.[21] Particularly, they have superior mechanical properties, high stability and melting points, good thermal shock resistance and low chemical reactivity. Many TMCs, such as Mo_2C, W_2C, WC, NbC and TaC also show superconductivity and excellent catalytic activity.[21–23] As one of the mostly studied TMCs, Mo_2C has high electron density at the Fermi level, affording high electronic conductivity and good nonlinear optical properties.[24,25] Mo_2C has two stable crystalline forms, orthorhombic α-Mo_2C and hexagonal β-Mo_2C, in which carbon atoms show distinct ordered and disordered distributions, respectively. It is nontrivial to prepare Mo_2C nanosheets with desired phase, controllable crystal size and uniform thickness. A few approaches were reported to prepare the graphene–Mo_2C heterostructures, and the superconductive as well as electrochemical properties have been investigated.[26–30] The graphene–Mo_2C hybrid film has been applied as a transparent electrode in a self-powered two-sided photodetector;[31] however, the optoelectronic properties particularly the associated electron transfer in such vertical heterostructures have not been fully explored.

Here, we present a highly responsive broadband photodetector using graphene-Mo_2C heterostructures grown by the chemical vapor deposition (CVD) process. The graphene–Mo_2C heterostructure photodetectors show significantly enhanced responsivity that is few orders of magnitude higher than that of the intrinsic graphene photodetectors in the visible range. Moreover, the heterostructure devices have a relatively

high responsivity at the telecommunication wavelength, which could fulfill increasing demands for photodetection at telecommunication bands.

The optical image in Fig. 1a shows the morphology of Mo_2C grown on a graphene sheet, which was pre-grown on a Cu foil *via* the CVD growth method. It reveals that Mo_2C sheets were uniformly grown on the graphene substrate. The graphene–Mo_2C heterostructure was transferred to the Si/SiO_2 substrate after etching away the Cu foil using $(NH_4)_2S_2O_8$. Fig. 1b shows the optical image of the graphene–Mo_2C heterostructure after being transferred to the SiO_2/Si substrate, in which we can clearly distinguish irregular shaped and bright Mo_2C sheets from the purple color graphene film at the bottom. Scanning electron microscope (SEM) image of the graphene–Mo_2C heterostructure is shown in Fig. 1c. It can see that the larger piece of the hexagonal Mo_2C sheet is ∼5 μm in width. Atomic force microscopy (AFM) was used to evaluate the topography and thickness of the Mo_2C sheet, as depicted in Fig. 1d and e. It is found that the surface of the Mo_2C sheet is very smooth and the thickness is about 8 nm. The high-resolution transmission electron microscopy (HRTEM) image of Mo_2C is shown in Fig. 1f, revealing the perfect atomic structure of the Mo_2C sheet without atomic scale defects. In particular, the selective area diffraction pattern (SAED) in the inset of Fig. 1f shows superlattice diffraction spots that are identical to that of α-Mo_2C,[30,32] which has an orthorhombic structure.

In order to reveal the stability of the graphene–Mo_2C heterostructure, the sample was annealed at 200 °C in ambient condition. Any difference in the heterostructure can be hardly seen from the optical images of the sample before (Fig. 2a) and
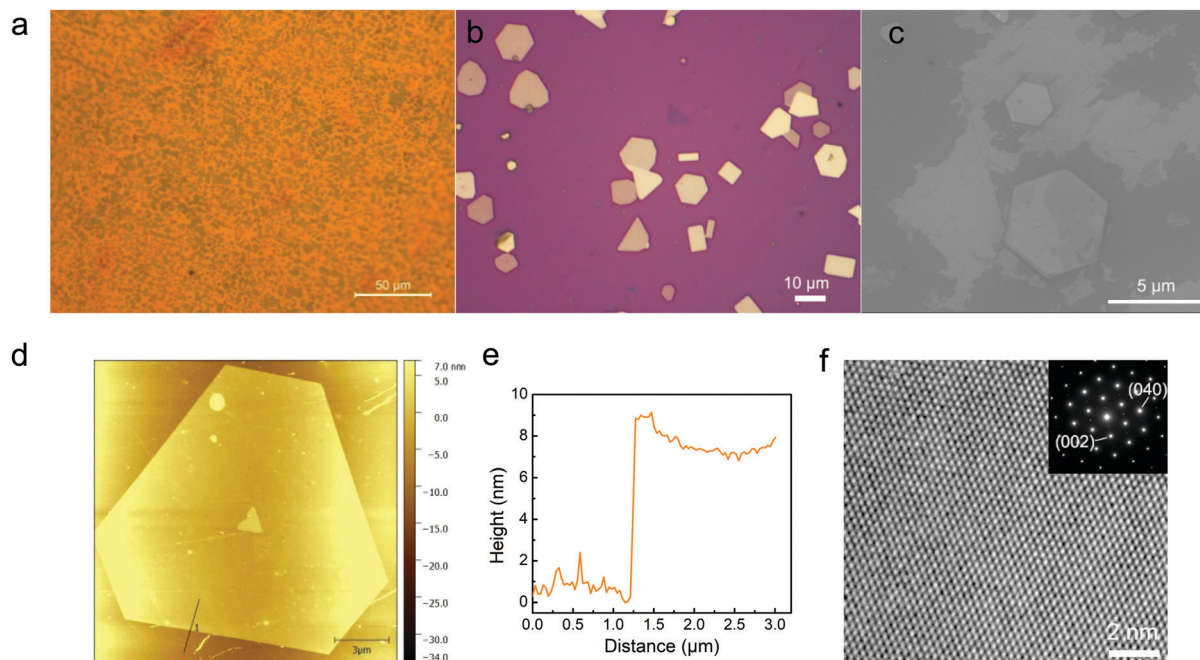

Fig. 1 (a) Optical image of graphene-Mo_2C grown on a Cu foil. (b) Optical image of graphene-Mo_2C after transferred to the Si/SiO_2 substrate. (c) SEM image of the graphene-Mo_2C heterostructure. (d) AFM topography of the graphene-Mo_2C heterostructure. (e) AFM cross-setional profile along the black line in (d). (f) HRTEM image of Mo_2C showing the atomic structure. The inset shows the SAED result.
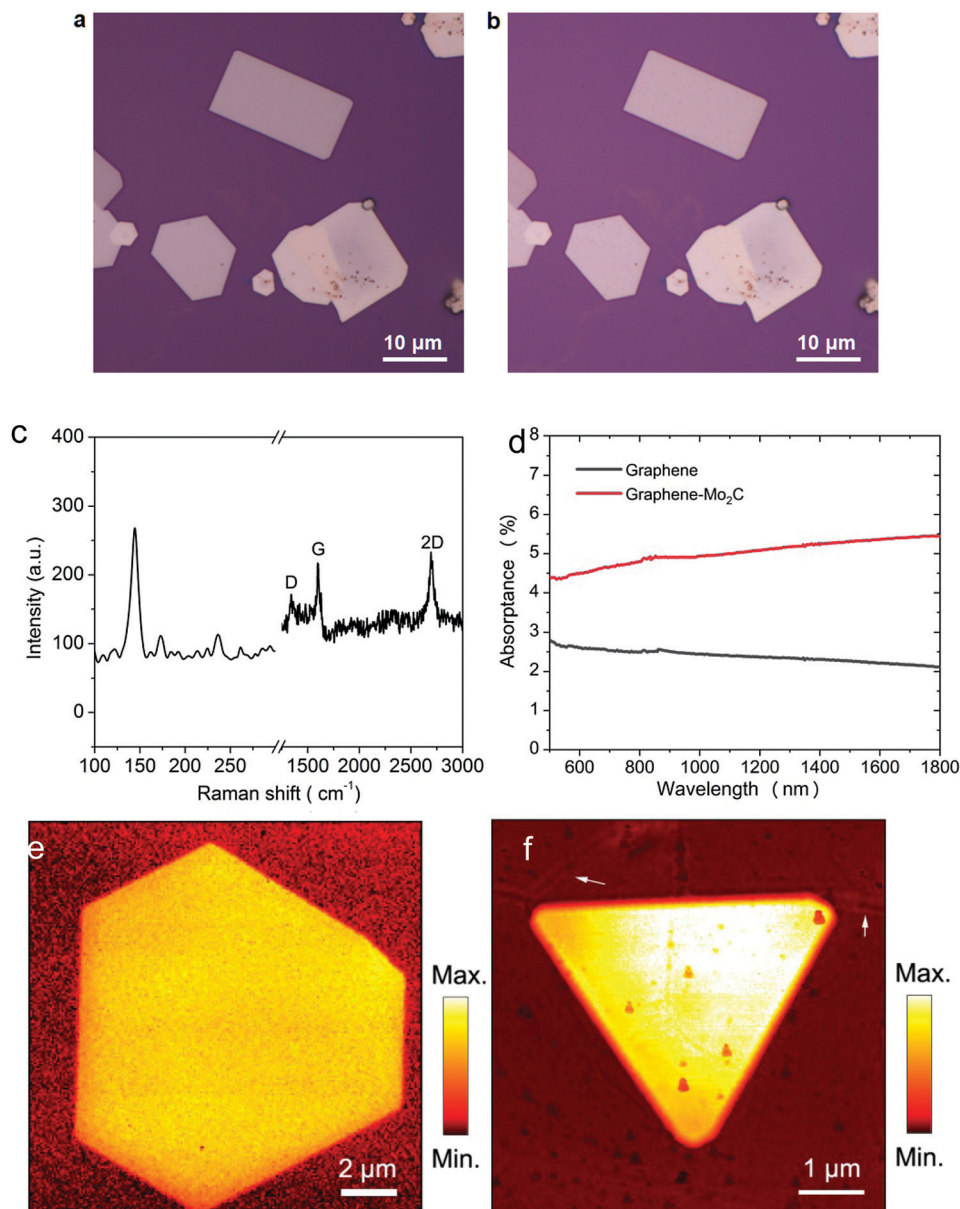
This journal is © the Owner Societies 2021

Phys. Chem. Chem. Phys., 2021, **23**, 23024–23031 | **23025**

Fig. 2 (a and b) Optical images of the graphene-Mo_2C heterostructure before (a) and after (b) annealing at 200 °C in ambient conditions. (c) Raman spectrum of the graphene-Mo_2C heterostructure with characteristic peaks of graphene and Mo_2C. (d) The optical absorption property of the graphene-Mo_2C heterostructure in comparison with that of graphene. (e) SNOM amplitude image of pure Mo_2C. (f) SNOM amplitude image of the graphene-Mo_2C heterostructure. The near-field amplitudes in (e) and (f) have been normalized to the substrates for comparison. The arrows in (f) indicate the plasmon fringes from the wrinkles or grain boundaries in graphene.

after (Fig. 2b) annealing. Fig. 2c shows the Raman spectrum of the graphene–Mo_2C heterostructure excited by a 633 nm laser. The peak of 149 cm^{-1} at the low frequency is the characteristic peak of Mo_2C, and the peaks at 1580 cm^{-1} and 2700 cm^{-1} are consistent with the G-band and 2D-band of graphene, respectively.[24,33] The optical absorption of the graphene–Mo_2C heterostructure thin film in comparison with graphene was also investigated, as shown in Fig. 2d. We can see that the graphene–Mo_2C heterostructure has an enhanced absorption over a wide wavelength range from 500 nm to 1800 nm, which is essential for broadband photodetection.

A scattering-type scanning near-field optical microscope (s-SNOM) was used to investigate the photocarriers of the heterostructure, as shown in Fig. 2e and f. More measurement details are provided in the Experimental section. The near-field image that is excited by the mid-infrared laser at 10.8 μm is capable of mapping the free-carrier distribution in the graphene–Mo_2C heterostructure and the pure Mo_2C sheet. It is clearly seen that the Mo_2C sheet on top of graphene looks brighter and has a few times higher near-field amplitude than the pure Mo_2C flake, which indicates larger localized carrier density. More photocarriers in the graphene–Mo_2C
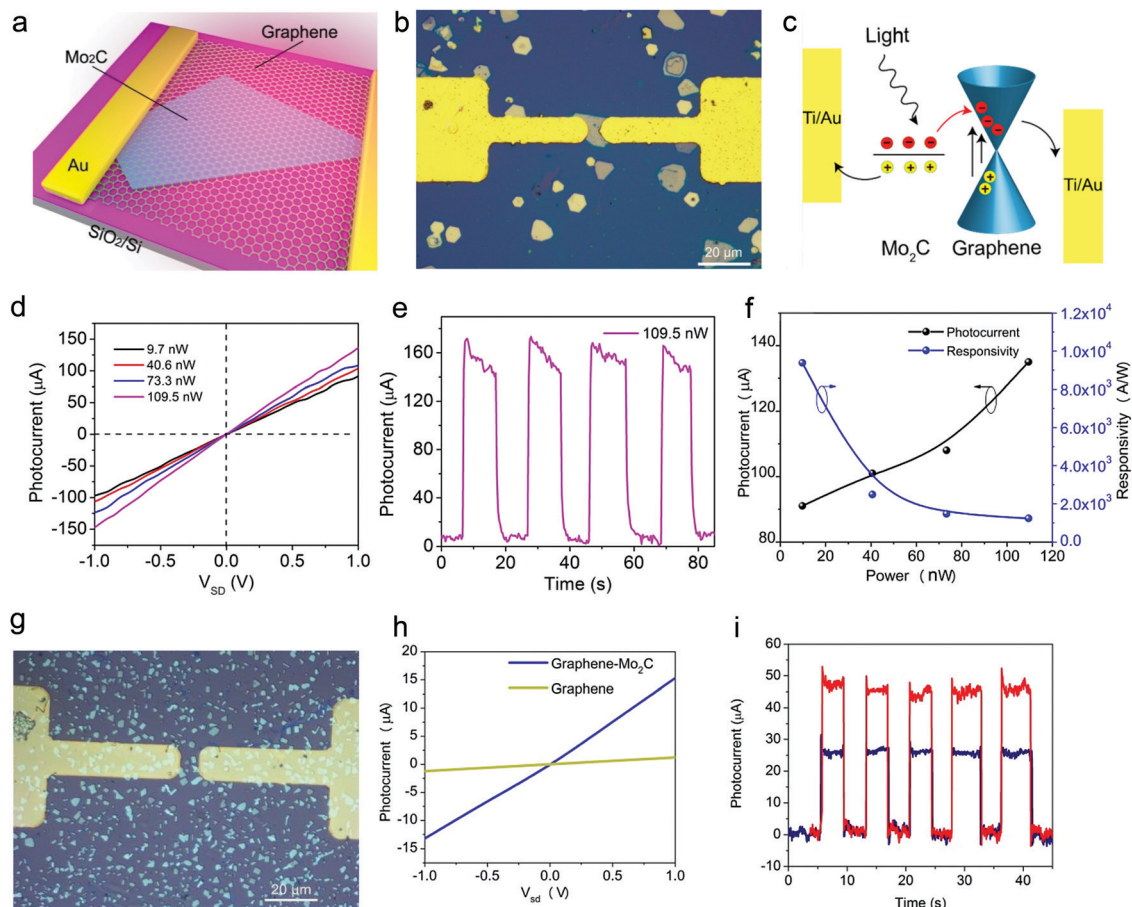
Fig. 3 (a) Schematic of the graphene-Mo$_2$C heterostructure photodetector device. (b) Optical image of the photodetector device on the Si/SiO$_2$ substrate showing the heterostructure with a large piece of Mo$_2$C sheet underneath graphene crossing the channel. (c) Band diagram of the graphene–Mo$_2$C heterostructure under illumination showing the transferring of photoexcited carriers. (d) The I−V curves of the graphene−Mo$_2$C device with large Mo$_2$C sheet illuminated by 405 nm laser under different laser powers. (e) The time-dependent photocurrent curve of the graphene−Mo$_2$C device with large Mo$_2$C sheet. V_{sd} = 1 V. Laser power: 109.5 nW. (d) Photocurrent and responsivity of the graphene−Mo$_2$C device with large Mo$_2$C sheet as a function of laser powers at 405 nm. (g) Optical image of the photodetector device on the Si/SiO$_2$ substrate showing a few small pieces of Mo$_2$C sheets in the channel. (h) The I−V curve of graphene−Mo$_2$C device with small Mo$_2$C sheets illuminated by 635 nm laser under laser power of 300 nW. (i) The time-dependent photocurrent curve of the graphene−Mo$_2$C device with small Mo$_2$C sheets. V_{sd} = 1 V. Laser power: 400 nW (black trace) and 500 nW (red trace).

heterostructure compared to intrinsic Mo$_2$C may result from the charge transfer between graphene and Mo$_2$C, which underpins the performance enhancement for photodetection.

We first study the photodetection of the graphene–Mo$_2$C heterostructure at the visible wavelengths, as presented in Fig. 3. The schematic of the graphene–Mo$_2$C heterostructure photodetector device on Si/SiO$_2$ is illustrated in Fig. 3a, and the optical image of a real device is shown in Fig. 3b. The graphene-Mo$_2$C heterostructure was applied as the channel material with a channel length of 8 μm and a width of 10 μm, in which graphene is on top of the Mo$_2$C sheets and gold electrodes are on top of graphene. As the Mo$_2$C sheet in the channel area has a large size, both the electrodes are contacted with graphene and Mo$_2$C sheet at the bottom. We proposed a schematic energy diagram to illustrate the movement of photoexcited carriers under illumination in the graphene–Mo$_2$C heterostructure, as depicted in Fig. 3c. Graphene is a semi-metal and Mo$_2$C is

metallic. The work function of graphene is 4.6 eV,[34] and the work function of Mo$_2$C is 4.75 eV.[35] While they are in contact, electrons will transfer from graphene to Mo$_2$C according to the simulation of charge density difference (Fig. S1, ESI†) until their Fermi levels are aligned together. Consequently, a built-in electrical field is formed as a result of balancing carrier concentrations at the junction. The work function of the graphene–Mo$_2$C heterostructure is calculated to be ~4.71 eV (see Fig. S1, ESI†). Under illumination, both graphene and Mo$_2$C can harvest incident light and generate photocarriers. With the help of the built-in electrical field in the heterostructure as well as external bias, the photocarriers are driven from Mo$_2$C to graphene and then transferred to two electrodes, leading to enhanced photocurrent.

Fig. 3d–f shows the photodetection results of the graphene–Mo$_2$C heterostructure consisting of a larger piece of the Mo$_2$C sheet. The photocurrent curves as a function of source-drain

bias was measured under the illumination of 405 nm light at different incident powers, as presented in Fig. 3d. The photocurrent increases linearly as V_{sd} varies from −1 to 1 V, suggesting Ohm's contact between the heterostructure and electrodes. Larger photocurrent is observed at higher light power, and the photocurrent can be effectively turned on and off with a relatively fast response, as depicted in Fig. 3e. The power-dependent photocurrent and responsivity are plotted in Fig. 3f. The photocurrent increases nonlinearly, while the incident power increases beyond 70 nW, and the corresponding photoresponsivity decreases exponentially with increasing power. The highest responsivity of 9381.4 A W^{-1} is observed

under the weakest light illumination (10 nW at 405 nm). Above 70 nW laser illumination, the responsivity reaches a state, and it reads as 1232.9 A W^{-1} at 110 nW.

To investigate the size effect of Mo$_2$C sheet on the photodetection performance, we fabricated a photodetector device on the graphene–Mo$_2$C heterostructure consisting of smaller pieces of Mo$_2$C sheets (size: 1–2 μm), as shown in Fig. 3g. Fig. 3h presents photocurrent as a function of source–drain voltage under illumination at a 635 nm laser with a power of 300 nW, and the photocurrent of the heterostructure is about 23 times higher than that of a pure graphene device. Nevertheless, the photocurrent of this device (about 10 μA) is about

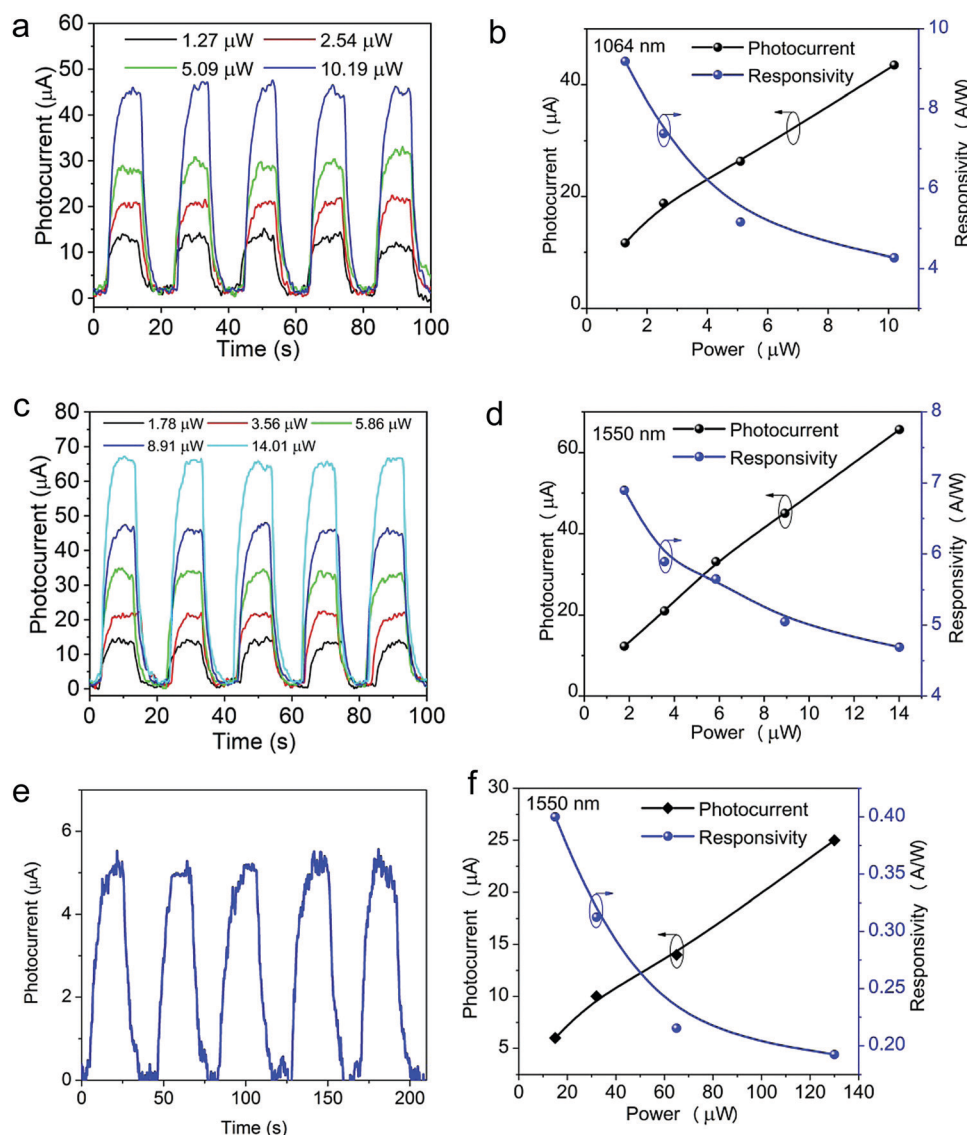**Fig. 4** (a) Time dependent photocurrent of the graphene–Mo$_2$C device with s large Mo$_2$C sheet tested at 1064 nm under different irradiation powers. Source–drain bias: 1 V, zero gate voltage. (b) Photocurrent and responsivity as a function of laser powers at 1064 nm for graphene–Mo$_2$C device with large Mo$_2$C sheet. (c) Time dependent photocurrent of the graphene–Mo$_2$C device with the large Mo$_2$C sheet tested at 1550 nm under different irradiation powers. Source–drain bias: 1 V, zero gate voltage. (d) Photocurrent and responsivity as a function of laser powers at 1550 nm for the graphene–Mo$_2$C device with the large Mo$_2$C sheet. (e) Time-dependent photocurrent of the graphene–Mo$_2$C device with small Mo$_2$C sheets tested at 1550 nm under the irradiation power of 15 μW. (f) Photocurrent and responsivity as a function of laser powers at 1550 nm for the graphene–Mo$_2$C device with small Mo$_2$C sheets.

23028 | *Phys. Chem. Chem. Phys.*, 2021, **23**, 23024–23031

This journal is © the Owner Societies 2021

ten times smaller than that of the device with a large piece of Mo$_2$C sheet ($\sim$100 μA, Fig. 3d) despite the difference in light power and wavelength. The time-dependent photocurrent curve was obtained under the illumination of 635 nm light using different laser power at fixed source–drain bias of 1 V, as shown in Fig. 3i. Similar to the above-mentioned observation, the graphene–Mo$_2$C photodetector can be effectively switched on and off with a rise time of 5.4 ms, and the photocurrent increases from 27 μA to 47 μA, when the laser power increases from 400 nW to 500 nW. The responsivity is calculated to be 94 A W^{-1} at the laser power of 400 nW, which is also ten times smaller than that of the device with a large piece of Mo$_2$C sheet (1232.9 A W^{-1} at 110 nW, Fig. 3f).

To further investigate the photodetection performance at the infrared range, we measured the heterostructure devices under the illumination of 1064 nm and 1550 nm lasers, as depicted in Fig. 4. For comparison, the devices consisting of both large Mo$_2$C sheet and smaller pieces of Mo$_2$C sheets have been studied. Fig. 4a and c show time-dependent photocurrent of the graphene-Mo$_2$C device with a large single Mo$_2$C sheet tested at 1064 nm and 1550 nm under different irradiation powers. The photocurrent can be turned on and off when the light is switched on and off, while larger light power gives higher photocurrent. As the thermal noise has an effect on the photocurrent, the photocurrent curve is not as straight as those measured at 405 nm and 635 nm. The photocurrent and responsivity as a function of illumination power are plotted in Fig. 4b and d. Similar power dependence to that in the visible range can be observed in infrared wavelengths. It is noteworthy to mention that the highest responsivity achieved is 9.2 A W^{-1} at 1064 nm and 6.9 A W^{-1} at 1550 nm, which is comparable to our previous report on other graphene heterostructures.[36] The photodetector based on graphene and smaller pieces of Mo$_2$C sheets was also measured at 1550 nm, and the results are shown in Fig. 4e and f. The trends of the power-dependent photocurrent and responsivity are similar to that of the device with graphene and large Mo$_2$C sheet but at relative lower scale. In particular, at the power of 15 μW, we can get a responsivity of 0.4 A W^{-1}, which is about 20 times smaller than that of the heterostructure device based on graphene and large Mo$_2$C sheet, but about 260 times higher than pure graphene device (1.5 mA W^{-1}).[5,6] We also compared our results with similar heterostructure devices consisting of graphene and other materials, as shown in Table S1 (ESI†). Based on the above-mentioned comparisons, we can conclude that the heterostructure device consisting of graphene and large Mo$_2$C sheet can deliver much better photodetection performance from visible to near-infrared wavelength ranges in terms of higher responsivity and shorter response time. This is because a large Mo$_2$C sheet can absorb more light and generate more photoexcited carriers, which can also be effectively injected into graphene and collected by two electrodes more efficiently due to shorter transport pathway.

Conclusions

In conclusion, we successfully demonstrated a highly responsive broadband photodetector based on the graphene–Mo$_2$C heterostructure that operates from visible to near-infrared telecommunication wavelengths. Because of the semi-metallic nature of both graphene and Mo$_2$C, the heterostructure has large photon absorption over a broad wavelength range. The construction of the vertical heterostructure allows an efficient transport of photoexcited carriers from Mo$_2$C to graphene so as to be collected by the electrodes. The heterostructure device with a large Mo$_2$C sheet exhibits not only broadband photodetection from the visible to telecommunication wavelengths, but also showed an ultrahigh photoresponsivity of 9381.4 A W^{-1} at 405 nm and relatively high responsivities at infrared wavelengths, i.e., 9.2 A W^{-1} at 1064 nm and 6.9 A W^{-1} at 1550 nm. The device is very durable as both materials have very good air stability. The demonstration of the unprecedented performance of the graphene–Mo$_2$C heterostructure photodetector may find intriguing potential for practical applications such as in optical sensing, biological imaging and optical communication.

Experimental section

CVD growth and transfer of graphene–Mo$_2$C crystals

A monolayer graphene film was first grown on a Cu foil (Alfa Aesar, 99.5% purity, 10 μm thick) according to previous reports.[37] Then, the foil was cut into 5 × 5 mm^2 pieces and placed on top of a Mo foil (Alfa Aesar, 99.95% purity, 100 μm thick) of the same size. The graphene/Cu/Mo sample was then placed in a quartz tube of outer diameter 25 mm and inner diameter 22 mm to act as the growth substrate for Mo$_2$C crystals. Subsequently, the graphene/Cu/Mo substrate was heated above 1085 °C in a horizontal tube furnace (Lindberg Bule M, TF55030C) under H$_2$ (200 sccm). A small amount of CH$_4$ (1.5 sccm) was then introduced into the reaction tube at ambient pressure to initiate the growth of 2D Mo$_2$C crystals on a graphene film, which usually lasted for 2–50 min. The longer the growth time, the larger the size of the ultrathin Mo$_2$C crystals. Finally, the sample was cooled down to room temperature at a cooling rate of 20–50 °C min^{-1} while maintaining the flow of CH$_4$ at the same rate.

A thin layer of poly (methyl methacrylate) (PMMA, weight-averaged molecular mass M_w = 600 000, 4 wt% in ethyl lactate) was first spin-coated onto the surface of Mo$_2$C/graphene samples at 5000 rpm for 1 min and cured at 180 °C for 30 min. The PMMA-coated samples were then immersed in a 0.2 M (NH$_4$)$_2$S$_2$O$_8$ solution at 70 °C for 10 min to etch away the Cu substrate. After that, the PMMA-coated Mo$_2$C/graphene samples were transferred onto the SiO$_2$/Si substrate. Finally, acetone was used to remove the PMMA layer and obtain the clean Mo$_2$C/graphene heterostructure film. The synthesis and transfer process of graphene-Mo$_2$C can also refer to previous report in ref. 30.

Characterizations of the graphene–Mo$_2$C heterostructure

The surface morphologies of the graphene–Mo$_2$C photodetectors were examined by SEM (Carl Zeiss, supra-55). The

This journal is © the Owner Societies 2021

Phys. Chem. Chem. Phys., 2021, **23**, 23024–23031 | **23029**

thicknesses of the graphene–Mo$_2$C heterostructures were measured *via* AFM (Bruker, Dimension Icon). The Raman spectra were collected using a micro-Raman system (Horiba Jobin Yvon, LabRAM HR 800) with a 514 nm excitation laser. Near-field optical images were captured using a commercial scattering type SNOM (NeaSNOM, NeaSpec GmbH) setup with a CO$_2$ laser (Edinburgh Instruments).

Device fabrication and photoelectric measurements

UV lithography was conducted to define the device pattern, electron-beam evaporation was performed to deposit gold (Au) contacts with a thickness of 100 nm, and a lift-off technique was used to form the source and drain electrodes on top of graphene. For the electrical transport measurement, a direct current (DC) bias voltage (1 V) was applied to one Au contact (source), allowing the source–drain current (I_{sd}) to flow through the graphene-BP heterostructure and reach the other Au contact (drain).

Optoelectronic measurements of the graphene–Mo$_2$C photodetector

The device characteristics measured at multiple wavelengths (405 nm, 635 nm, 1064 nm and 1550 nm) were performed by using a probe station (Cascade M150) equipped with a semiconductor property analyzer (Keithley 4200). All the measurements were performed at room temperature under ambient conditions.

Author contributions

X. B. and T. S. contributed equally to this work. W. R., Q. B. and H. S. supervised the project. X. B. and T. S. planned and performed most of the experiments. C. X., S. L., J. G. and W. R. contributed to material synthesis and characterizations. Y. L., J. G., Y. Z., S. B. N., G. X. and S. L. contributed to device fabrication and photocurrent measurements. X. B., T. S., Y. L., W. R., Q. B. and H. S. analyzed the data and co-wrote the paper. All authors discussed the results and commented on the manuscript. All authors have approved the final version of the manuscript.

Conflicts of interest

There are no conflicts to declare.

Acknowledgements

Notes and references

1 Q. Bao, H. Zhang, B. Wang, Z. Ni, C. H. Y. X. Lim, Y. Wang, D. Y. Tang and K. P. Loh, *Nat. Photonics*, 2011, **5**, 411–415.

2 M. Liu, X. Yin, E. Ulin-Avila, B. Geng, T. Zentgraf, L. Ju, F. Wang and X. Zhang, *Nature*, 2011, **474**, 64–67.

3 S. Bae, H. Kim, Y. Lee, X. Xu, J. S. Park, Y. Zheng, J. Balakrishnan, T. Lei, H. R. Kim and Y. I. Song, *Nat. Nanotechnol.*, 2010, **5**, 574–578.

4 N. M. Gabor, J. C. Song, Q. Ma, N. L. Nair, T. Taychatanapat, K. Watanabe, T. Taniguchi, L. S. Levitov and P. Jarillo-Herrero, *Science*, 2011, **334**, 648–652.

5 T. Mueller, F. Xia and P. Avouris, *Nat. Photonics*, 2010, **4**, 297–301.

6 F. Xia, T. Mueller, Y.-M. Lin, A. Valdes-Garcia and P. Avouris, *Nat. Nanotechnol.*, 2009, **4**, 839–843.

7 R. R. Nair, P. Blake, A. N. Grigorenko, K. S. Novoselov, T. J. Booth, T. Stauber, N. M. Peres and A. K. Geim, *Science*, 2008, **320**, 1308.

8 K. I. Bolotin, K. J. Sikes, Z. Jiang, M. Klima, G. Fudenberg, J. Hone, P. Kim and H. L. Stormer, *Solid State Commun.*, 2008, **146**, 351–355.

9 S. Morozov, K. Novoselov, M. Katsnelson, F. Schedin, D. Elias, J. A. Jaszczak and A. Geim, *Phys. Rev. Lett.*, 2008, **100**, 016602.

10 F. H. Koppens, D. E. Chang and G. D. A. Fj, *Nano Lett.*, 2011, **11**, 3370–3377.

11 T. Echtermeyer, L. Britnell, P. Jasnos, A. Lombardo, R. Gorbachev, A. Grigorenko, A. Geim, A. C. Ferrari and K. Novoselov, *Nat. Commun.*, 2011, **2**, 1–5.

12 M. Furchi, A. Urich, A. Pospischil, G. Lilley, K. Unterrainer, H. Detz, P. Klang, A. M. Andrews, W. Schrenk and G. Strasser, *Nano Lett.*, 2012, **12**, 2773–2777.

13 A. Splendiani, L. Sun, Y. Zhang, T. Li, J. Kim, C.-Y. Chim, G. Galli and F. Wang, *Nano Lett.*, 2010, **10**, 1271–1275.

14 O. Lopez-Sanchez, D. Lembke, M. Kayci, A. Radenovic and A. Kis, *Nat. Nanotechnol.*, 2013, **8**, 497–501.

15 K. Roy, M. Padmanabhan, S. Goswami, T. P. Sai, G. Ramalingam, S. Raghavan and A. Ghosh, *Nat. Nanotechnol.*, 2013, **8**, 826–830.

16 A. Gao, E. Liu, M. Long, W. Zhou, Y. Wang, T. Xia, W. Hu, B. Wang and F. Miao, *Appl. Phys. Lett.*, 2016, **108**, 223501.

17 K. Kam and B. Parkinson, *J. Phys. Chem.*, 1982, **86**, 463–467.

18 K. F. Mak, C. Lee, J. Hone, J. Shan and T. F. Heinz, *Phys. Rev. Lett.*, 2010, **105**, 136805.

19 M. Naguib, O. Mashtalir, J. Carle, V. Presser, J. Lu, L. Hultman, Y. Gogotsi and M. W. Barsoum, *ACS Nano*, 2012, **6**, 1322–1331.

20 M. Naguib, V. Mochalin, M. W. Barsoum and Y. Gogotsi, *Adv. Mater.*, 2014, **26**, 992–1005.

21 L. Toth, *Transition metal carbides and nitrides*, Elsevier, 2014.

22 N. Morton, B. James, G. Wostenholm, D. Pomfret, M. Davies and J. Dykins, *J. Less-Common Met.*, 1971, **25**, 97–106.

23 R. Willens, E. Buehler and B. Matthias, *Phys. Rev.*, 1967, **159**, 327.

24 H. Mu, M. Tuo, C. Xu, X. Bao, S. Xiao, T. Sun, L. Li, L. Zhao, S. Li and W. Ren, *Opt. Mater. Express*, 2019, **9**, 3268–3276.

25 C. Xu, L. Wang, Z. Liu, L. Chen, J. Guo, N. Kang, X.-L. Ma, H.-M. Cheng and W. Ren, *Nat. Mater.*, 2015, **14**, 1135–1141.

26 W. Sun, X. Wang, J. Feng, T. Li, Y. Huan, J. Qiao, L. He and D. Ma, *Nanotechnology*, 2019, **30**, 385601.

27 S. Chaitoglou, P. Tsipas, T. Speliotis, G. Kordas, A. Vavouliotis and A. Dimoulas, *J. Cryst. Growth*, 2018, **495**, 46–53.

28 R. Deng, H. Zhang, Y. Zhang, Z. Chen, Y. Sui, X. Ge, Y. Liang, S. Hu, G. Yu and D. Jiang, *Chin. Phys. B*, 2017, **26**, 067901.

29 D. Geng, X. Zhao, Z. Chen, W. Sun, W. Fu, J. Chen, W. Liu, W. Zhou and K. P. Loh, *Adv. Mater.*, 2017, **29**, 1700072.

30 C. Xu, S. Song, Z. Liu, L. Chen, L. Wang, D. Fan, N. Kang, X. Ma, H.-M. Cheng and W. Ren, *ACS Nano*, 2017, **11**, 5906–5914.

31 Z. Kang, Z. Zheng, H. Wei, Z. Zhang, X. Tan, L. Xiong, T. Zhai and Y. Gao, *Sensors*, 2019, **19**, 1099.

32 Y. Fan, C. Xu, X. Liu, C. Ma, Y. Yin, H.-M. Cheng, W. Ren and X. Li, *NPG Asia Mater.*, 2020, **12**, 1–9.

33 A. C. Ferrari, J. C. Meyer, V. Scardaci, C. Casiraghi, M. Lazzeri, F. Mauri, S. Piscanec, D. Jiang, K. S. Novoselov and S. Roth, *Phys. Rev. Lett.*, 2006, **97**, 187401.

34 Y. Shi, K. K. Kim, A. Reina, M. Hofmann, L.-J. Li and J. Kong, *ACS Nano*, 2010, **4**, 2689–2694.

35 R. Wilson and W. McKee, *J. Appl. Phys.*, 1967, **38**, 1716–1718.

36 T. Sun, Y. Wang, W. Yu, Y. Wang, Z. Dai, Z. Liu, B. N. Shivananju, Y. Zhang, K. Fu and B. Shabbir, *Small*, 2017, **13**, 1701881.

37 Y. Zhu, S. Murali, W. Cai, X. Li, J. W. Suk, J. R. Potts and R. S. Ruoff, *Adv. Mater.*, 2010, **22**, 3906–3924.